Journal of Alloys and Compounds 967 (2023) 171766

Contents lists available at ScienceDirect

Journal of Alloys and Compounds

journal homepage: www.elsevier.com/locate/jalcom

Two-dimensional gadolinium-doped ceria nanosheets for low temperature sintering of solid oxide fuel cells barrier layer

Leticia P.R. Moraes [a], Marina Machado [a], Lays N. Rodrigues [a], Ziqi Sun [b], Debora Marani [c], Fabio C. Fonseca [a,*]

[a] Nuclear and Energy Research Institute, IPEN-CNEN, São Paulo, Brazil
[b] Queensland University of Technology, Brisbane, Australia
[c] Addifab ApS, Mårkærvej 2, 2630 Taastrup, Denmark

ARTICLE INFO

Keywords:
Gadolinium-doped ceria
2D doped-ceria
Coprecipitation synthesis
Barrier layer
SOFC

ABSTRACT

A novel method for bottom-up synthesis of two-dimensional (2D) gadolinium-doped cerium oxide (CGO) nanosheets is developed and demonstrated as an efficient precursor for interdiffusion barrier layer deposition in solid oxide fuel cells. The CGO is the standard material used as an interlayer in intermediate-temperature solid oxide fuel cells to avoid undesirable reactions between lanthanum strontium cobalt ferrite (LSCF) cathode and yttria-stabilized zirconia (YSZ) electrolyte materials. Herein, the shape-control of the 2D CGO by a low-cost wet-chemical method allowing for the fabrication of fully dense barrier layer of CGO is reported. The high surface coverage promoted by the 2D CGO nanosheets resulted in a thin (~ 1 μm) and dense interdiffusion barrier layer sintered at 1150 °C preventing the undesirable reaction between oxide ion conducting phases occurring at higher temperatures. The electrochemical properties of solid oxide fuel cells confirmed the CGO nanosheet as an efficient layer for preventing the formation of resistive phases at the electrolyte/cathode interface.

1. Introduction

Solid oxide fuel cells (SOFCs) have great potential in providing clean energy with high electrical efficiency. However, to become more economically attractive, considerable efforts are being made in order to minimize their degradation, reduce their cost, and improve their performance [1–3]. An important strategy to minimize the cost of SOFC and increase the durability is to lower both processing and operation temperatures [4–6]. Decreasing the sintering temperature of the materials and reducing the SOFC operating temperatures to intermediate temperatures (IT-SOFC) are current challenges for the cell's scalable production. However, at intermediate temperatures (500 – 750 °C) the electrochemical reactions and charge transport are less efficient [7–10].

To enable lower operating temperatures, it is necessary to decrease the electrolyte's resistance and increase the catalytic activity of the electrodes. Studies have been made regarding the reduction of electrolyte thickness, the substitution of yttria-stabilized zirconia (YSZ) electrolyte to other ionic conductors such as gadolinium-doped ceria (CGO) [8,11], and the replacement of the LSM (strontium-doped lanthanum manganite) cathode by a more active material such as LSCF (lanthanum strontium cobalt iron oxide) [12,13]. However, there are still problems associated with these materials. The CGO exhibits mixed ionic and electronic properties at high temperatures and cation interdiffusion between the LSCF and the YSZ can occur during sintering and cell operation, resulting in the formation of resistive phases such as $La_2Zr_2O_7$ and $SrZrO_3$ [14].

An alternative SOFC configuration that allows the use of the state-of-the-art YSZ electrolyte together with the highly active LSCF cathode is the introduction of a diffusion barrier layer between the YSZ electrolyte and the cathode. The role of this layer is to avoid the migration of cations at the interface between the electrolyte and cathode [15,16]. The material of choice is CGO, a good ion conductor and compatible with the other materials in the cell. However, from 1000 °C, Zr diffuses into the CGO layer, and, at temperatures higher than 1200 °C, Ce diffuses into the YSZ electrolyte [17]. These two interdiffusion processes result in more resistive phases and cause severe degradation of SOFC performance. Therefore, to produce a thin, dense, and continuous layer of CGO over the YSZ electrolyte, without causing undesired reactions, the sintering temperature of the components must be as low as possible. In order to achieve these requirements, an interesting approach is to tailor

* Corresponding author.
E-mail address: fabiocf@usp.br (F.C. Fonseca).

https://doi.org/10.1016/j.jallcom.2023.171766
Received 20 May 2023; Received in revised form 19 July 2023; Accepted 14 August 2023
Available online 15 August 2023

the surface morphology of the CGO layer.

Two-dimensional (2D) nanomaterials (nanosheets, nanobelts, nanoflakes) exhibit a high specific surface area, a low level of porosity and can provide good coverage of surfaces even if made as an ultra-thin film. Moreover, the functional properties of the 2D CGO enable the production of an effective barrier that can be sintered at a lower temperature with the other components of the multilayered cell without producing additional undesired phases. Many strategies have been proposed for the synthesis of 2D nanomaterials including hydrothermal, electrochemical deposition, pulsed laser deposition, and aqueous exfoliation [18–20]. In this study, we developed a low-temperature and easily scalable coprecipitation synthesis of CGO with a sheet-like structure, configuring a pioneering one-pot process for CGO nanosheets fabrication. The synthesized material and the deposition method were evaluated as a dense and thin (~ 1 μm) CGO effective barrier layer between YSZ and LSCF in a solid oxide fuel cell.

2. Experimental

2.1. Synthesis

Gadolinium-doped (10 mol%) cerium oxide nanosheets (CGONS) were prepared by a coprecipitation method with sodium hydroxide (NaOH). An aqueous solution of cerium nitrate $Ce(NO_3)\cdot 6\ H_2O$ (99 %, Sigma-Aldrich) and gadolinium nitrate $Gd(NO_3)\cdot 6\ H_2O$ (99 %, Sigma-Aldrich) was prepared by dissolving the salts in deionized water to make a total cationic concentration of 0.03 M, considering the $Ce_{0.9}Gd_{0.1}O_{1.95}$ composition. Hexamethylenetetramine (HMTA, 99 %, Sigma-Aldrich, 2 M) was used as the nucleating agent, using 1:2 molar ratio (metal salt: HMTA). To prepare the solution, 20 mL of the HMTA solution was slowly added into 400 mL cerium-gadolinium nitrate solution, under stirring. The solution was kept at 10 °C for 4 days in a closed dedicated refrigerator, with coupled thermostat, under static conditions. After the low temperature treatment, the solution was mixed with 40 mL of ethylene glycol under magnetic stirring for 20 min at room temperature. Then, 80 mL of 0.6 M NaOH was slowly added (for 30 min) under vigorous stirring. As the NaOH is added, the clear solution turns into a translucent brown suspension. The suspension was aged in an oven at 90 °C for 24 h. The purple precipitate formed was washed/centrifuged with deionized water five times and dried at 80 °C overnight. The material was deagglomerated in an agate mortar and calcined at 500 °C for 1 h, using a heating rate of 2 °C•min^{-1}.

2.2. Electrochemical cells fabrication

Symmetrical cells and electrolyte-supported cells with CGONS were fabricated. First, to produce the CGONS ink, 20 mg of the ceramic powder were solubilized in 160 mL of a water-ethanol mixture (2:1 vol.), under ultrasonic bath for 30 min, keeping the bath temperature lower than 40 °C. When a translucent suspension was obtained, 10 g of polyvinylpyrrolidone (PVP) were added under sonication to increase the viscosity of the ink, resulting in a colloidal suspension of CGONS that was used to deposit the barrier layer. To ensure that the nanosheets were well dispersed in the suspension, the ink was sonicated for 5 min before its use.

To fabricate the LSCF|CGONS|YSZ symmetric cells, the CGONS ink was deposited on YSZ substrates via the spin-coating technique (spin coater, Laurel, model WS-400-6NPP-LITE) at a rotation rate of 2500 rpm for 10 s, followed by drying at 100 °C for 30 min. This process was repeated five times. Furthermore, to evaluate the effectiveness of the CGONS as a barrier layer, a LSCF commercial ink (Fuel Cell Materials) was applied by the spin coater at a rotation of 3000 rpm for 10 s. The samples were then calcined in air at 500 °C for 1 h and sintered at 1150 °C for 1 h. Ageing of the cells with a LSCF layer was carried out ex-situ in a resistive box-type oven, at 900 °C for 90 h. Reference samples produced with commercial CGO (PRAXAIR) were produced in the same conditions (by solubilization of the commercial powder in water-ethanol and adjusting the viscosity with PVP).

Electrolyte supported solid oxide fuel cells were prepared using YSZ pellets. To produce the pellets, the YSZ powder (Tosoh) was transferred into a circular mold (25 mm) and a uniaxial compression of 60 MPa was applied for 60 s. The pellets were then sintered at 1500 °C for 5 h. The final diameter and thickness of the pellets were 18 mm and 400 μm, respectively. A slurry of NiO/YSZ was deposited on one side of the electrolyte by spin coating, as described elsewhere [21,22]. The CGONS (or CGO commercial as the reference) and LSCF ink were deposited at the other side of the electrolyte as previously mentioned. The fuel cell was sintered at 1150 °C for 1 h.

2.3. Characterization

The morphology of the as-prepared materials was analyzed by scanning electron microscopy (SEM; Tescan MIRA3 microscopy) operating at an accelerating voltage of 3 kV. X-rays diffraction (XRD) patterns were collected in a Rigaku MiniFlex (Rigaku Corporation, U.S.A.) diffractometer in the 2θ° range of 20–80 °. Thermogravimetric analyses (TGA) were carried out in a Setaram LabSys equipment using a heating rate of 10 °Cmin^{-1} in the 25–1200 °C temperature range under synthetic air flow. Cylindrical pellets were prepared using the calcined powders (500 °C for 1 h) by uniaxial pressing for dilatometry analysis (Setaram Labsys), carried out between room temperature and 1400 °C, with a heating rate of 10 °C·min^{-1} under synthetic air flow of 50 mL·min^{-1}.

The electrical properties of the symmetrical cells were evaluated by electrochemical impedance spectroscopy (EIS). Gold paste was applied to the parallel surfaces of the symmetrical cells and cured at 800 °C for 1 h. The symmetrical cells with the following configurations were obtained: Au|LSCF|YSZ and Au|LSCF|CGONS|YSZ. The samples were inserted into a chamber with alumina capillaries and platinum wires for electrical contact, then placed in a vertical resistive oven, with a controlled atmosphere. Measurements were performed by a Solartron SI 1260 frequency analyzer, in a frequency range of 10 MHz to 1 Hz at an ac amplitude of 100 mV. Data acquisition and processing were performed using the ZPlot/ZView program.

The electrochemical properties of the electrolyte-supported cells with CGONS or commercial CGO layer were tested in an open flange test set-up from Fiaxell SOFC Technologies™. The current collection was carried out by gold wires connected to a gold mesh (diameter 37 mm) in the air side and by a nickel mesh on the fuel side. The electrochemical measurements were carried out at 800 °C under H_2 and synthetic air, both with a flow rate of 12 L·h^{-1}, by using a PARSTAT® 3000A-DX electrochemical workstation. The EIS data were measured at open circuit voltage (OCV) in the 1 MHz - 1 Hz frequency range with an ac amplitude of 10 mV. Current-voltage curves were measured from OCV to 0.4 V at a rate of 10 mV·s^{-1}.

3. Results and discussions

3.1. Synthesis and characterization of the CGONS

Fig. 1 shows images of both the precursor solution and the obtained CGO nanosheets (CGONS). Fig. 1a shows images of the cerium and gadolinium nitrates solution with HMTA, after the low temperature (10 °C) treatment, taken at different times during the 24 h of the coprecipitation step. The slow hydrolysis of the HMTA at 10 °C was able to promote a gradual increase of the pH of the solution, allowing a better control of the reaction products. NaOH was then slowly added, under vigorous stirring, to the precursor solution to promote the coprecipitation of the CGO nanosheets (CGONS). As the pH of the medium increases from 6.9 to 12.4, the solution becomes cloudy, from transparent to translucent brown, and at the end of the NaOH addition, the suspension is opaque. After ageing at 90 °C for 24 h, the precipitate formed has purple color, which can be attributed to the formation of intermediate

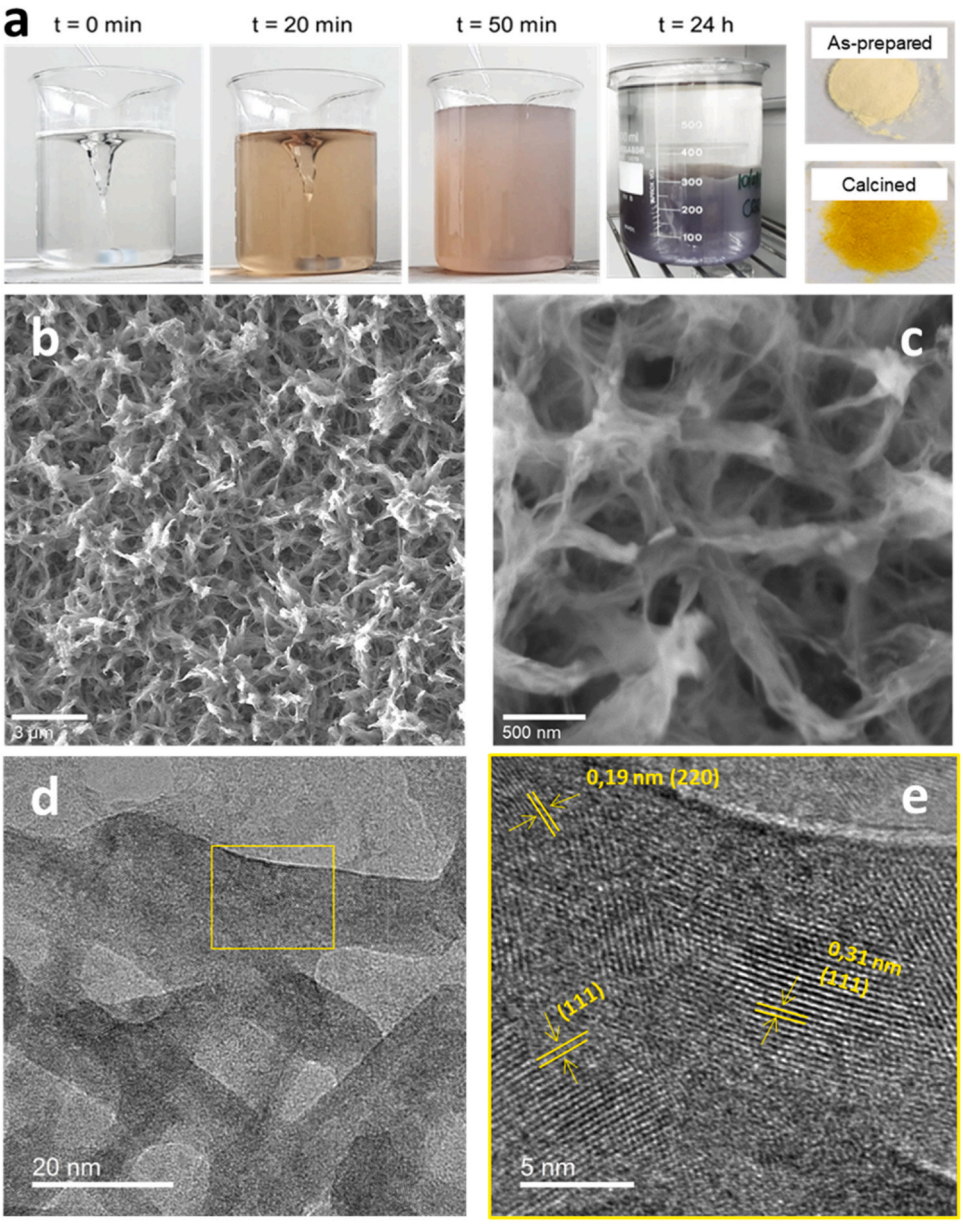

Fig. 1. Images of the CGO solution during coprecipation synthesis using NaOH and obtained CGO powders (a). SEM images of the as-prepared CGONS (b and c), TEM (d), and HRTEM (e) images of the calcined CGONS.

species, such as cerium hydroxides. It is noted that the Ce^{3+} is less stable in air or alkaline conditions than Ce^{4+}; therefore, the observed color may also indicate the formation of the intermediate $Ce(OH)_3$ [23]. However, after washing and drying the powder at 80 °C overnight, the sample turns pale yellow, suggesting that the intermediates have been converted to cerium oxide. Upon calcining at 500 °C, a dark yellow powder is obtained. Scanning electron microscopy (SEM) images of the CGONS at different stages of synthesis are shown in the Supplementary Information Fig. S1. The images collected at different stages indicate that the morphology does not change considerably during the process, showing a good stability of the 2D shape.

Figs. 1b and 1c show the scanning electron microscopy (SEM) images at different magnifications of the as-produced CGONS. The SEM images evidenced an interconnected net of nearly translucid nanoparticles with sheet-like morphology. Transmission electron microscopy (TEM) and high-resolution TEM (HRTEM) were used to analyze the morphology of the CGONS after calcining at 500 °C, as shown in Figs. 1d and 1e. The 2D morphology of the CGO was confirmed, indicating that the particle shape is essentially preserved after calcining. Fig. 1e shows that the nanosheets preferentially expose the CGO (111) crystal plane, corresponding to the 0.31 nm distance measured between the interference fringes.

Thermogravimetric analysis (TGA) was carried out to investigate the thermal decomposition process of the as-prepared sample. Fig. 2a shows that mass loss develops at temperatures < 500 °C. The DTG curve shows three main degradation processes at 70, 150 and 230 °C. The total mass loss of the sample at 1200 °C is 13 % and refers mainly to absorbed water evaporation. The TGA data confirm that the sample can be calcined at relatively low temperature (~500 °C).

Fig. 2b shows the XRD patterns of both the as-prepared and the calcined (500 °C) samples. The XRD of the as-prepared material reveals that the sample is crystalline with broad peaks indexed as the cubic CGO phase. All diffraction patterns confirm the formation of the fluorite CGO with diffraction peaks corresponding to planes (111), (200), (220), (311), (222), (400), and (331). For the as-prepared sample, peaks corresponding to $Ce(OH)_3$ were observed, indicating the hydroxide as an

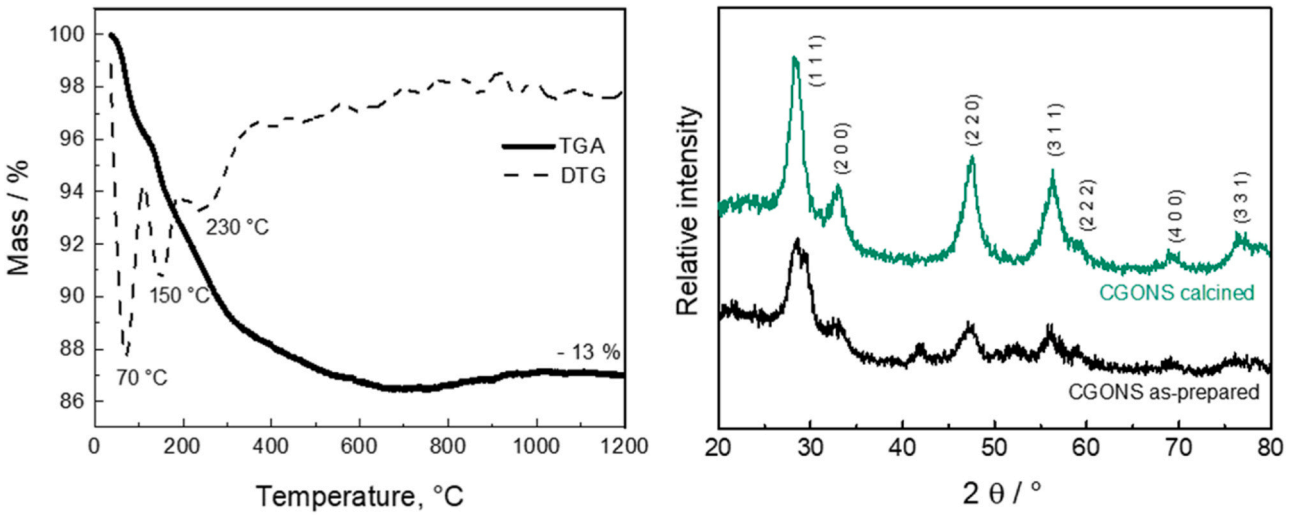

Fig. 2. Thermogravimetric analysis of the as-prepared CGONS (left panel). X-ray diffraction patterns of the as-prepared and the calcined CGONS (right panel).

intermediate phase during the reaction. Due to the color changes of the solution observed during the reaction, the formation of $Ce(OH)_3$ was expected. Previous studies [24] on the production of CeO_2 from cerium nitrate and NaOH, using different Ce^{3+}/OH^- ratios, observed the formation of precipitated $Ce(OH)_3$ as a reaction intermediate, which is oxidized to ceria by increasing the temperature during an autoclave treatment. Similarly, after calcining at 500 °C, no other crystalline impurities or intermediates, such as $Ce(OH)CO_3$ and $Ce(OH)_3$, were detected by XRD, indicating that single phase CGO is obtained.

3.2. Evaluation of the CGONS as an electrolyte/barrier layer

Processing of oxides usually requires high temperature sintering to achieve targeted mechanical and microstructural properties (grain size, porosity, etc.). To determine the sintering temperature of the dried powder of CGONS dilatometric runs of uniaxially pressed pellets were conducted. Fig. 3 displays the densification and densification rate curves of the CGONS calcined powder. The CGONS sample exhibited a low green density of 30 % initially, owing to its loosely packed structure. However, it achieved 92 % relative density at 1400 °C, indicating a significant level of densification. This high densification, despite the low starting green density, can be attributed to the dominant influence of surface diffusion effects on the sintering behavior, surpassing the impact of the initial packing density [25]. The onset of linear shrinkage, associated with densification of the ceramic, is observed at 900 °C. The total linear retraction develops up to ~ 1200 °C when the material reaches a densification plateau. A typical densification process can be observed by analyzing the densification rate curve, where a progressive single-step shrinkage achieves its maximum densification rate at 1100 °C. This behavior is attributed to a uniform particle size distribution and high surface energy of the ceramic powder with good sintering activity. As compared to the nanosheets, the commercial CGO powder exhibits a lower activation energy sintering processes, starting at 800 °C, but a lower maximum densification is achieved despite the higher green density. The final relative apparent density of 80 % of commercial CGO is attributed to the refractory behavior of ceria-based oxides [25].

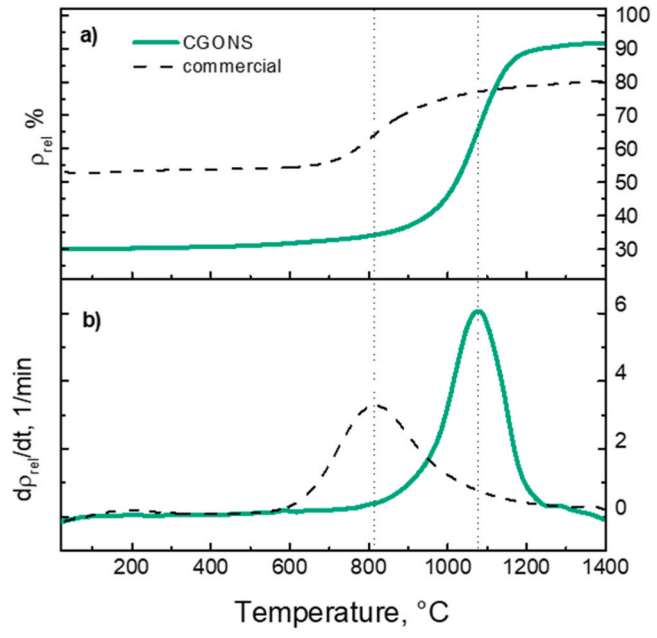

Fig. 3. Densification curve (a) and densification rate curve (b) of CGONS and commercial CGO pellets.

Taking advantage of both the synthesis method and properties of nanosheets, a colloidal ink was developed to expand the use of such material as a functional layer. The calcined CGONS powder, water, and ethanol as solvents, and PVP as the polymeric binder were combined to optimize the rheological properties to obtain a stable suspension with no apparent sedimentation of the ink. SEM images of the ink are shown in Fig. S2 of the Supplementary Information. The amount of PVP added is crucial to adjust the viscosity resulting in homogeneous coating and to avoid pores and cracks during the drying process. The PVP concentration was kept as low as possible, and the spin coating process was repeated to reach the desired final thickness, with drying steps between each deposition. Fig. 4a shows images of the ink, where the Tyndall effect can be observed by irradiating the ink with a laser beam, confirming the colloidal nature of the solution. The thermogravimetric analysis of the ink determined the decomposition temperature of the organic compounds to occur in successive steps from room temperature up to 400 °C. Fig. 4c presents the X-ray diffraction pattern of the CGONS ink, with all the characteristic peaks of the fluorite CGO structure. After deposition and drying, the deposited layer over the YSZ substrate exhibits the CGO peaks, indicating the successful deposition of a thin CGO layer. By using the spin coating technique, a homogeneous layer of nanosheets is applied with a higher packing density than in the uniaxially pressed powder used in the dilatometry run. The CGO nanosheets tend to orient themselves in the same direction, resulting in a uniform film over the YSZ surface, as evidenced by the Supplementary Fig. S3. In the EDS mapping (Fig. 4d) of the sample calcined at 500 °C, the

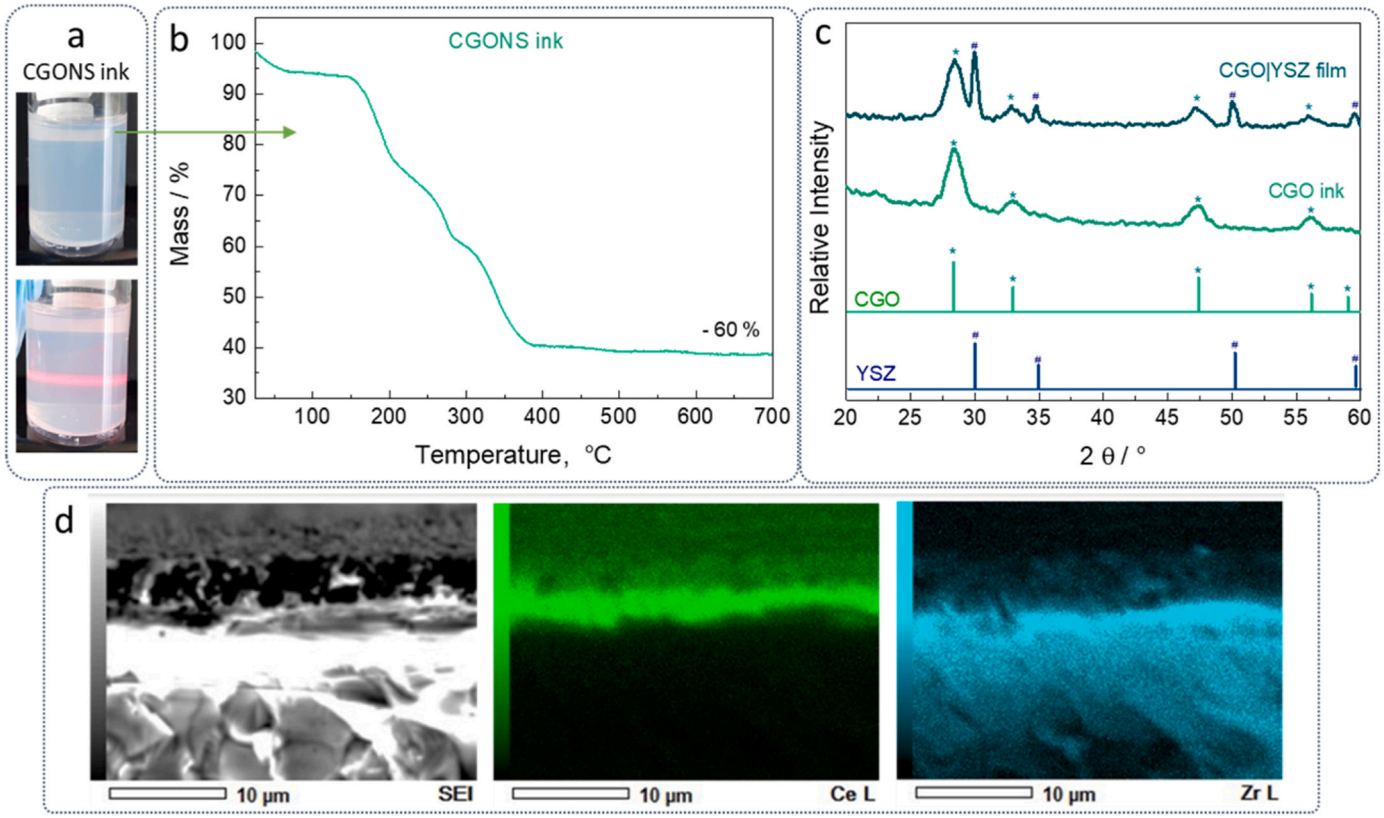

Fig. 4. CGONS ink showing the Tyndall effect (a). Thermogravimetric analysis of the ink (b). X-rays diffraction patterns of the ink and the substrate after the ink deposition and calcination (c). Scanning electron microscopy image and corresponding EDS mapping showing the CGO layer deposited on YSZ substrate (d).

composition of the layer is confirmed. A continuous layer of ceria deposited on the YSZ substrate indicates that the spin coating process and the sintering were efficient to produce a CGO layer with the desired properties.

The initial results evidenced a uniform and continuous layer of CGO over the YSZ substrate obtained at sintering temperatures below 1200 °C. Such a low sintering temperature resulting in a dense CGO layer is a benchmark usually attained by physical deposition methods to avoid the formation of resistive phases between the SOFC components [26–30]. Thus, the CGONS were further analyzed in SOFC as an inter-diffusion barrier layer between the LSCF cathode and the YSZ electrolyte.

To simulate the cathode/electrolyte interface, and the degradation caused during the SOFC processing and operation, the CGONS barrier layer was deposited between a YSZ substrate and LSCF electrode in symmetrical cells. The LSCF|CGONS|YSZ|CGONS|LSCF assembly was sintered at 1150 °C for 1 h. A control sample without the barrier layer (LSCF|YSZ|LSCF) was prepared under the same conditions for comparison. Both symmetrical cell samples, with and without the CGONS layer, were heat treated at 900 °C for 90 h to intentionally induce a fast degradation by the LSCF and YSZ reaction. The electrochemical properties of the symmetrical cells, both fresh sintered and thermally degraded, were studied by EIS. Fig. 5 shows the EIS diagrams of the symmetric cells measured at 790 °C with and without the CGONS barrier layer as-sintered (t = 0 h) and after ageing (900 °C for 90 h) in air.

The experimental EIS data of the symmetric cells of Fig. 5 were fitted with the equivalent circuit $LR_{\Omega}(R_{P1}CPE_{P1})(R_{P2}CPE_{P2})$, where L is the inductive contribution due to the measurement system, R_{Ω} (ohmic resistance) is the series resistance attributed to the contributions of electrical conductivity (current collector electronics and ionic electrolyte YSZ), while $R_{Pi}CPE_{Pi}$ refers to the polarization impedance of the cathode. Table 1 presents the area-specific resistance results obtained by

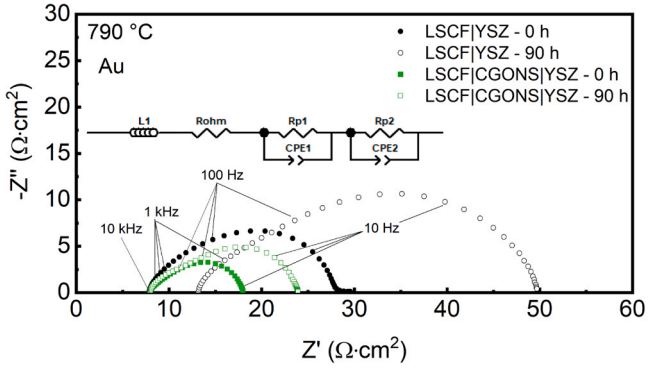

Fig. 5. Impedance diagrams obtained at 790 °C for Au|LSCF|YSZ and Au|LSCF|CGONS|YSZ symmetric cells before and after ageing at 900 °C. The equivalent circuit model used for fitting EIS data is depicted in the panel.

Table 1
Fitted series resistances (R_{Ω}) and polarization resistances (R_{P1} and R_{P2}) of symmetric cells Au|LSCF|YSZ and Au|LSCF|CGONS|YSZ before (0 h) and after (90 h) ageing at 900 °C extracted from EIS data.

Sample - aging	R_{Ω} (Ω.cm²)	R_{P1} (Ω.cm²)	R_{P2} (Ω.cm²)
LSCF|YSZ - 0 h	7.7	7.7	12.5
LSCF|YSZ - 90 h	12.9	10.1	26.9
LSCF|CGO|YSZ - 0 h	7.7	3.6	6.7
LSCF|CGO|YSZ - 90 h	7.7	4.5	11.6

EIS fitting. The EIS diagrams revealed that the sample with the CGONS barrier layer was considerably less affected by ageing at 900 °C. It is important to note that the R_{Ω}, determined at the high frequency

intercepet of the diagram with real axis, of the as-sintered symmetric cells showed the same value irrespective of the CGONS layer. Such result indicates that CGONS represent no additional ohmic resistance to the cell, a feature related to the high density of the layer and lack of solid solution between YSZ and CGO due to the low sintering temperature. The sample with CGONS exhibited the same R_Ω before and after the thermal ageing, suggesting that the applied barrier layer was effective in preventing unwanted reactions at the electrode/electrolyte interface. On the other hand, the symmetric cell without the barrier layer showed pronounced increase in R_Ω, attributed to a degradation of the charge transfer process at the electrode/electrolyte interface. Usually, this increase in R_Ω is related to the formation of insulating phases such as $SrZrO_3$ at the interface, mainly due to the diffusion of Sr in the electrolyte [28]. In the polarization component related to the electrode's resistance (R_{pol}) it is observed that the samples with the barrier layer show an increase of 25 % after ageing, while the samples without a barrier layer displayed a significantly higher polarization increase (~ 45 %). Two main components are observed in the R_{pol} of the EIS diagram: one at high frequencies (> 10^3 Hz), and another at low frequencies (< 10^3 Hz). Previous studies have shown that the component at high frequencies is attributed to ionic diffusion at the electrolyte/cathode interface, while the low-frequency component is ascribed to the transport and reduction of O_2 on the surface of the material [31]. In the sample with the CGONS layer, the increase in R_{pol} is observed mainly in the low-frequency component. Such a R_{pol} increase is possibly related to a microstructural evolution of the LSCF at 900 °C. On the contrary, the sample without the barrier layer, the increase in R_{pol} is observed in both components revealing an extensive degradation of the electrochemical properties of the electrode, possibly associated with the interdiffusion and reaction between LSCF and YSZ [32].

Energy dispersive X-rays (EDX) analysis was carried out on the electrolyte of the samples after thermal ageing of the cells. Fig. 6 shows the EDX spectra and the related SEM images of the symmetric cells. The sample without the CGONS barrier layer exhibits a higher intensity of the Sr signal compared to the sample with the CGONS barrier layer. The quantitative EDX results presented in Table 2 show an approximately two-fold higher weight percentage (wt%) of Sr in the LSCF|YSZ cell compared to the LSCF|CGONS|YSZ cell. Additionally, the presence of La is observed in the LSCF|YSZ electrolyte, further supporting the effectiveness of the CGONS in preventing cation interdiffusion. The SEM images of the cross section of the symmetric cell confirm that the CGO layers inhibits the cation interdiffusion in the interface, as shown by the smoother surfaces of the ceramic grains in sample with the CGONS (Fig. 6c), as compared to that of YSZ in Fig. 6b.

Table 2
Composition of the interface determined by energy dispersive X-ray (normalized of the elements present at the at YSZ electrolyte close the interface of both the LSCF|YSZ and LSCF|CGONS|YSZ symmetric cells after ageing at 900 °C.

Sample	Zr wt%	Y wt%	Sr wt%	La wt%
LSCF/YSZ - 90 h	52.22	11.66	7.75	1.62
LSCF/CGO/YSZ - 90 h	63.42	12.83	3.53	–

The electrochemical properties of the diffusion barrier layer between the YSZ electrolyte and the LSCF cathode were evaluated in an YSZ electrolyte-supported single cell, with Ni/YSZ anode and LSCF cathode. The cathode sintering was conducted after the CGONS deposition at 1150 °C. To compare the performance of the barrier layer produced with the CGONS synthesized in the present study, a reference single cell with a barrier layer prepared with commercial CGO was prepared following the same procedure, keeping the same mass of CGO deposited and sintering temperature. Lowering the sintering temperature for the production of dense layers of CGO is usually done by adding sintering additives such as Fe_2O_3 [33] and CuO [34], or by using more sophisticated deposition techniques, such as physical techniques such as PLD (pulsed laser deposition) [35,36] and PVD (physical vapor deposition) [37,38], which exhibit best reported performances. Using a 2D CGO layer prepared by a chemical method is an important innovation to obtain dense films of CGO as a barrier layer (or bielectrolyte) for SOFC. Fig. 7 shows the SEM images of the cross-sections of the cathode/electrolyte interface of single cells produced with a barrier layer of commercial CGO and CGONS.

The SEM micrographs in Fig. 7a show that the sintering temperature of 1150 °C was insufficient to produce a dense CGO layer from the commercial material. The commercial layer produced has high porosity and ~ 2 μm final thickness. On the other hand, the CGONS layer, Fig. 7b, exhibits high densification in the same sintering condition, and consequently lower thickness (~ 1 μm). Both CGO layers are homogeneous, without defects, and show good adhesion to the adjacent component layers.

The SOFC polarization curves obtained at 800 °C using H_2 as fuel are shown in Fig. 8a. The cell with CGONS barrier layer presented an open circuit potential value OCV = 1.1 V, close to the theoretical value expected by the Nernst potential [39]. The unit cell produced with commercial CGO barrier layer had a slightly lower OCV value, OCV = 1 V.

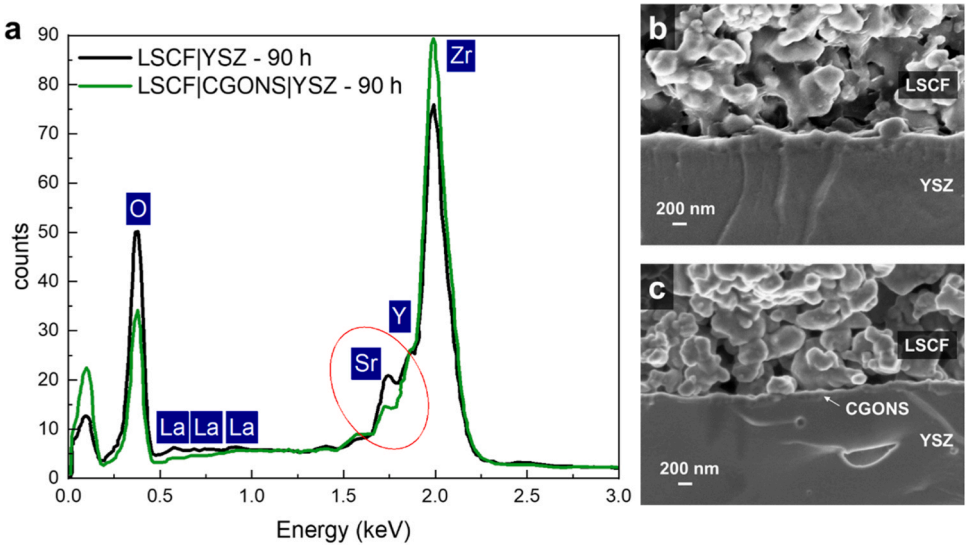

Fig. 6. (a) Energy dispersive X-ray spectra at the electrolyte at the interface of the LSCF|YSZ and LSCF|CGONS|YSZ half cells after ageing at 900 °C, and respective SEM images at (b) and (c).

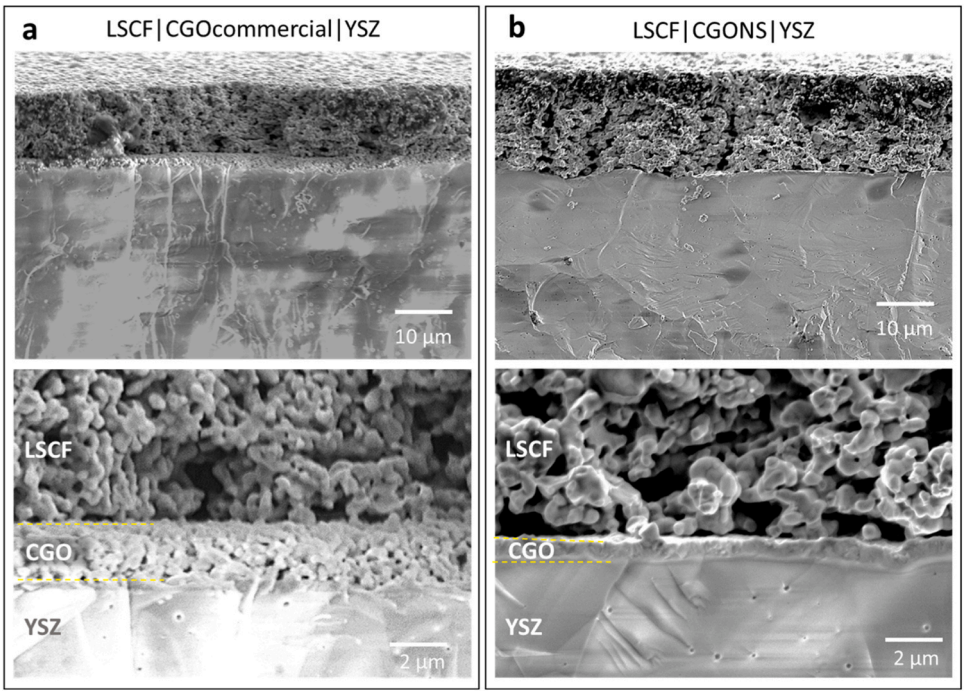

Fig. 7. SEM images with different magnifications of the cross-sections of single SOFC produced with barrier layer of commercial CGO (a) and CGONS (b), sintered at 1150 °C for 1 h.

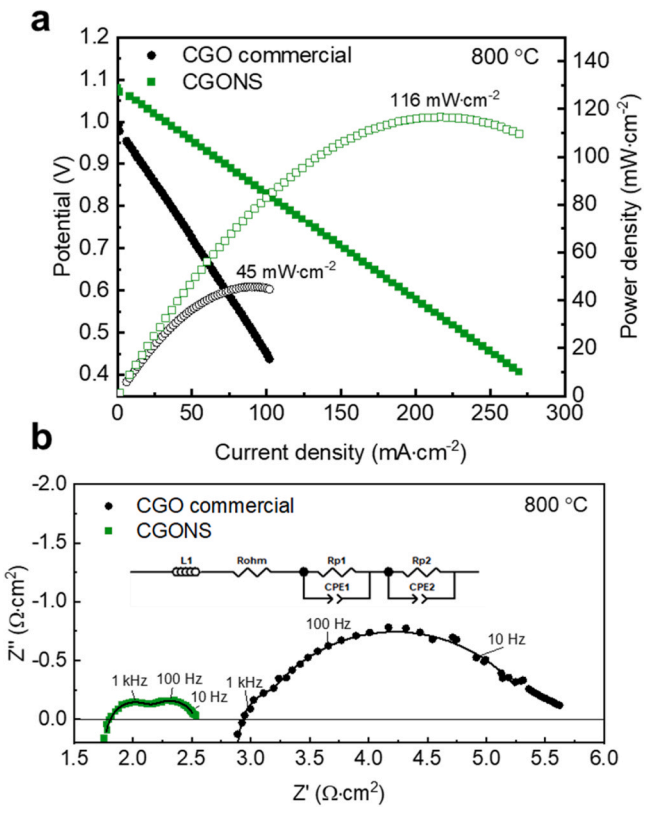

Fig. 8. (a) Polarization curves of single cells produced with barrier layer of commercial CGO and CGONS, measured at 800 °C, using H_2 as fuel and (b) impedance diagrams of the cells at OCV.

However, the OCV difference of the samples should not be attributed to the barrier layer, but rather to a fabrication effect of the ceramic cells or the measuring setup. Both samples exhibit linear polarization curves that show the ohmic drop as the main polarization source. Indeed, the sample with porous (commercial) CGO barrier layer exhibits a much more pronounced polarization due to ohmic resistance than that of the CGONS.

Considering that the electrical resistance of the electrolyte is the main contribution of the ohmic drop polarization and that both YSZ supports are identical, the main difference is attributed to the barrier layer of CGO. The sintering of CGONS resulted in a layer with higher density and lower thickness, which contributed to higher electrical conductivity of the electrolyte/cathode interface of this sample. Cell power outputs are lower than state-of-the-art SOFCs as thick YSZ electrolytes (~ 700 µm) are used, but the tested fuel cells aim at investigating the properties of the CGO layers rather than achieving optimized performance. The maximum power density reached by the fuel cell produced with a CGONS barrier layer was 2.5 times higher than that of the cell with commercial CGO. Cathode sintering at 1150 °C may have caused the formation of insulating phases at the YSZ/LSCF interface of the fuel cell with commercial CGO. The formation of $La_2Zr_2O_7$ and $SrZrO_3$ is facilitated in porous barrier layers, as this microstructure allows the diffusion of species (La and Sr) from the LSCF cathode to the YSZ electrolyte [28].

The EIS diagrams measured at the OCV (Fig. 8b) were fitted with the same equivalent circuit as the symmetric cells, $LR_{\Omega}(R_{P1}CPE_{P1})(R_{P2}CPE_{P2})$. The cell produced with a commercial CGO barrier layer has $R_{\Omega} \sim 3\ \Omega{\cdot}cm^2$, a value almost two-fold higher than the R_{Ω} of the cell with CGONS, in good agreement with the polarization curve ohmic drop. This result is directly related to the larger thickness and lower density of the commercial CGO layer, which results in higher ohmic contact resistance in this sample. The EIS diagram reveals R_{pol} components with at least two discernible contributions on the semicircle arcs, a higher frequency contribution (~ 1 kHz) and another occurring at lower frequencies (< 100 Hz). The R_{pol} of the two samples shows important differences in the electrode processes of the cells. It is interesting to note that this difference is particularly more pronounced in the low-frequency portion of the diagram (R_{P2}), which is much more resistive in the commercial CGO sample. The $R_{P2} \sim 0.42\ \Omega{\cdot}cm^2$ of the cell with CGONS is considerably smaller than the $R_{P2} \sim 2.32\ \Omega{\cdot}cm^2$ of the

commercial CGO. These characteristics are in perfect agreement with data measured for the symmetric cells (Fig. 5) indicating that the CGONS layer contributed to more active electrodes with a greater extent of the triple-phase boundary (TPB) in which the oxygen reduction reactions are facilitated at the CGO/LSCF interface. On the contrary, the thicker and porous layer of commercial CGO is not effective to avoid reaction between YSZ and LSCF, decreasing the contact of the cathode with the electrolyte and hindering the charge transport processes in the TPB.

The electrochemical properties of the single fuel cells showed that the 2D morphology of nanosheets is very efficient for applications that require uniform coating and good densification at lower temperatures. The experiments carried out showed that the control of precursor morphology can be a strategy for the manufacture of devices. Indeed, the results of the present study confirm that nanosheets are efficient for covering surfaces by homogeneous layers with controllable thickness and dense microstructure.

4. Conclusions

A facile approach to synthesize crystalline CGO nanosheets, approaching a 2D morphology, produced by coprecipitation method without any surfactant or template is reported. A low calcining temperature allows such material to be redissolved, keeping its morphology, in different suspension formulations with great stability and flexibility to process with low-cost and scalable deposition techniques. The two-dimensional material is shown to have the desired structure to be deposited as a thin and dense layer on to solid electrolytes, achieving high density at relatively low temperature that avoids either robust equipment or sintering additives. The 2D ceria layers were applied as diffusion barrier layers in single solid oxide fuel cells supported on the YSZ electrolyte and were efficient in preventing the formation of resistive phases at the LSCF electrolyte/cathode interface. Thus, the innovative method for 2D CGO has a great potential for numerous applications such as energy conversion, catalysts and optically or electrically active functional materials.

CRediT authorship contribution statement

Leticia P. R. Moraes: Methodology, Investigation, Writing – original draft. **Marina Machado:** Investigation, Writing – review & editing. **Lays N. Rodrigues**: Investigation. **Ziqi Sun:** Methodology, Conceptualization, Supervision. **Debora Marani:** Conceptualization, Supervision and **Fabio C. Fonseca:** Supervision, Writing – review & editing, Funding acquisition, Project administration.

Declaration of Competing Interest

The authors declare that they have no known competing financial interests or personal relationships that could have appeared to influence the work reported in this paper. Fabio Coral Fonseca reports financial support was provided by State of Sao Paulo Research Foundation. Fabio Coral Fonseca reports financial support was provided by National Council for Scientific and Technological Development. Leticia P. R. Moraes reports financial support was provided by Coordination of Higher Education Personnel Improvement and National Council for Scientific and Technological Development.

Data availability

Data will be made available on request.

Acknowledgements

The authors are thankful for the support of the Brazilian CNEN, CAPES (88881.187628/2018-01), CNPq (Sis-H_2 407967/2022-2 and 141740/2016-7), and FAPESP (2017/11937-4, 2019/04499-6, 2022/06295-1). FCF is a CNPq fellow (304485/2022-5). DM and ZS were visiting scientists in Brazil funded by FAPESP (2015/20434-0, 2016/50339-2). Authors are thankful to Frederic Charlot and Marlu Cesar Steil (University-Grenoble-Alpes), Vincenzo Esposito (DTU), and Daniel Z. de Florio (UFABC) for EDX analysis and fruitful discussions.

Appendix A. Supporting information

Supplementary data associated with this article can be found in the online version at doi:10.1016/j.jallcom.2023.171766.

References

[1] P.A. Connor, X. Yue, C.D. Savaniu, R. Price, G. Triantafyllou, M. Cassidy, G. Kerherve, D.J. Payne, R.C. Maher, L.F. Cohen, R.I. Tomov, B.A. Glowacki, R. V. Kumar, J.T.S. Irvine, Tailoring SOFC electrode microstructures for improved performance, Adv. Energy Mater. 8 (2018) 1800120, https://doi.org/10.1002/aenm.201800120.

[2] L. Fan, B. Zhu, P.-C. Su, C. He, Nanomaterials and technologies for low temperature solid oxide fuel cells: recent advances, challenges and opportunities, Nano Energy 45 (2018) 148–176, https://doi.org/10.1016/j.nanoen.2017.12.044.

[3] S.A. Saadabadi, A. Thallam Thattai, L. Fan, R.E.F. Lindeboom, H. Spanjers, P. V. Aravind, Solid oxide fuel cells fuelled with biogas: potential and constraints, Renew. Energy 134 (2019) 194–214, https://doi.org/10.1016/j.renene.2018.11.028.

[4] D.J.L. Brett, A. Atkinson, N.P. Brandon, S.J. Skinner, Intermediate temperature solid oxide fuel cells, Chem. Soc. Rev. 37 (2008) 1568, https://doi.org/10.1039/b612060c.

[5] S.U. Costilla-Aguilar, M.I. Pech-Canul, M.J. Escudero, R.F. Cienfuegos-Pelaes, J. A. Aguilar-Martínez, Gadolinium doped ceria nanostructured oxide for intermediate temperature solid oxide fuel cells, J. Alloy. Compd. 878 (2021), 160444, https://doi.org/10.1016/j.jallcom.2021.160444.

[6] R. Fuentes, R. Baker, Synthesis and properties of Gadolinium-doped ceria solid solutions for IT-SOFC electrolytes, Int. J. Hydrog. Energy 33 (2008) 3480–3484, https://doi.org/10.1016/j.ijhydene.2007.10.026.

[7] C. Nicollet, J. Waxin, T. Dupeyron, A. Flura, J.-M. Heintz, J.P. Ouweltjes, P. Piccardo, A. Rougier, J.-C. Grenier, J.-M. Bassat, Gadolinium doped ceria interlayers for Solid Oxide Fuel Cells cathodes: enhanced reactivity with sintering aids (Li, Cu, Zn), and improved densification by infiltration, J. Power Sources 372 (2017) 157–165, https://doi.org/10.1016/j.jpowsour.2017.10.064.

[8] H. Inaba, Ceria-based solid electrolytes, Solid State Ion. 83 (1996) 1–16, https://doi.org/10.1016/0167-2738(95)00229-4.

[9] A.V. Coles-Aldridge, R.T. Baker, Ionic conductivity in multiply substituted ceria-based electrolytes, Solid State Ion. 316 (2018) 9–19, https://doi.org/10.1016/j.ssi.2017.12.013.

[10] B.S. Kang, A. Inoishi, A. Takagaki, T. Ishihara, $Pr_2Ni_{0.71}Cu_{0.24}Ga_{0.05}O_4$-$Sm_{0.2}Ce_{0.8}O_{1.9}$ composite film as active cathodic layer for intermediate temperature solid oxide fuel cells, Solid State Ion. 327 (2018) 59–63, https://doi.org/10.1016/j.ssi.2018.10.027.

[11] B. Steele, Appraisal of $Ce_{1-y}Gd_yO_{2-y/2}$ electrolytes for IT-SOFC operation at 500°C, Solid State Ion. 129 (2000) 95–110, https://doi.org/10.1016/S0167-2738(99)00319-7.

[12] A. Esquirol, N.P. Brandon, J.A. Kilner, M. Mogensen, Electrochemical characterization of $La_{0.6}Sr_{0.4}Co_{0.2}Fe_{0.8}O_3$ cathodes for intermediate-temperature SOFCs, J. Electrochem. Soc. 151 (2004) A1847, https://doi.org/10.1149/1.1799391.

[13] S. Jiang, A comparison of O2 reduction reactions on porous (La,Sr)MnO_3 and (La,Sr)(Co,Fe)O_3 electrodes, Solid State Ion. 146 (2002) 1–22, https://doi.org/10.1016/S0167-2738(01)00997-3.

[14] S.P. Jiang, Development of lanthanum strontium cobalt ferrite perovskite electrodes of solid oxide fuel cells – a review, Int. J. Hydrog. Energy 44 (2019) 7448–7493, https://doi.org/10.1016/j.ijhydene.2019.01.212.

[15] D. Szymczewska, J. Karczewski, A. Chrzan, P. Jasinski, CGO as a barrier layer between LSCF electrodes and YSZ electrolyte fabricated by spray pyrolysis for solid oxide fuel cells, Solid State Ion. 302 (2017) 113–117, https://doi.org/10.1016/j.ssi.2016.11.008.

[16] H. Fan, M. Keane, P. Singh, M. Han, Electrochemical performance and stability of lanthanum strontium cobalt ferrite oxygen electrode with gadolinia doped ceria barrier layer for reversible solid oxide fuel cell, J. Power Sources 268 (2014) 634–639, https://doi.org/10.1016/j.jpowsour.2014.03.080.

[17] R. Knibbe, J. Hjelm, M. Menon, N. Pryds, M. Søgaard, H.J. Wang, K. Neufeld, Cathode-electrolyte interfaces with CGO barrier layers in SOFC: cathode-electrolyte interfaces in IT-SOFCs, J. Am. Ceram. Soc. 93 (2010) 2877–2883, https://doi.org/10.1111/j.1551-2916.2010.03763.x.

[18] Z. Sun, T. Liao, Y. Dou, S.M. Hwang, M.-S. Park, L. Jiang, J.H. Kim, S.X. Dou, Generalized self-assembly of scalable two-dimensional transition metal oxide nanosheets, Nat. Commun. 5 (2014), 3813, https://doi.org/10.1038/ncomms4813.

[19] Z. Yang, Z. Wu, Y. Lyu, J. Hao, Centimeter-scale growth of two-dimensional layered high-mobility bismuth films by pulsed laser deposition, InfoMat 1 (2019) 98–107, https://doi.org/10.1002/inf2.12001.

[20] D. Marani, L.P.R. Moraes, F. Gualandris, S. Sanna, D.Z. de Florio, V. Esposito, F. C. Fonseca, Nucleation front instability in two-dimensional (2D) nanosheet gadolinium-doped cerium oxide (CGO) formation, CrystEngComm 20 (2018) 1405–1410, https://doi.org/10.1039/C7CE01737E.
[21] S.D. da Nobrega, N.K. Monteiro, F. Tabuti, D.Z. de Florio, F.C. Fonseca, Optimization of spin-coated electrodes for electrolyte-supported solid oxide fuel cells, Matéria 22 (2017), https://doi.org/10.1590/s1517-707620170001.0136.
[22] R. Muccillo, E.N.S. Muccillo, F.C. Fonseca, Y.V. França, T.C. Porfirio, D.Z. de Florio, M.A.C. Berton, C.M. Garcia, Development and testing of anode-supported solid oxide fuel cells with slurry-coated electrolyte and cathode, J. Power Sources 156 (2006) 455–460, https://doi.org/10.1016/j.jpowsour.2005.06.021.
[23] D. Zhang, H. Fu, L. Shi, J. Fang, Q. Li, Carbon nanotube assisted synthesis of CeO_2 nanotubes, J. Solid State Chem. 180 (2007) 654–660, https://doi.org/10.1016/j.jssc.2006.11.025.
[24] M. Lin, Z.Y. Fu, H.R. Tan, J.P.Y. Tan, S.C. Ng, E. Teo, Hydrothermal synthesis of CeO_2 nanocrystals: ostwald ripening or oriented attachment? Cryst. Growth Des. 12 (2012) 3296–3303, https://doi.org/10.1021/cg300421x.
[25] V. Esposito, A. Kabir, M. Rosa, N.V. Nong, T.S. Rodrigues, L.N. Rodrigues, M.F. S. Machado, L.P.R. Moraes, D. Marani, F.C. Fonseca, Tuning diffusion paths in shaped ceria nanocrystals, CrystEngComm 21 (2019) 4025–4029, https://doi.org/10.1039/C9CE00414A.
[26] A. Tsoga, A. Gupta, A. Naoumidis, D. Skarmoutsos, P. Nikolopoulos, Performance of a double-layer CGO/YSZ electrolyte for solid oxide fuel cells, Ionics 4 (1998) 234–240, https://doi.org/10.1007/BF02375951.
[27] H. Xu, K. Cheng, M. Chen, L. Zhang, K. Brodersen, Y. Du, Interdiffusion between gadolinia doped ceria and yttria stabilized zirconia in solid oxide fuel cells: Experimental investigation and kinetic modeling, J. Power Sources 441 (2019), 227152, https://doi.org/10.1016/j.jpowsour.2019.227152.
[28] R. Kiebach, W.-W. Zhang, W. Zhang, M. Chen, K. Norrman, H.-J. Wang, J. R. Bowen, R. Barfod, P.V. Hendriksen, Stability of $La_{0.6}Sr_{0.4}Co_{0.2}Fe_{0.8}O_3$/$Ce_{0.9}Gd_{0.1}O_2$ cathodes during sintering and solid oxide fuel cell operation, J. Power Sources 283 (2015) 151–161, https://doi.org/10.1016/j.jpowsour.2015.02.064.
[29] V. Esposito, D.W. Ni, D. Marani, F. Teocoli, K.T. Sune Thydén, D.Z. De Florio, F. C. Fonseca, Accelerated ceria–zirconia solubilization by cationic diffusion inversion at low oxygen activity, J. Mater. Chem. A 4 (2016) 16871–16878, https://doi.org/10.1039/C6TA06308J.
[30] F.C. Fonseca, S. Uhlenbruck, R. Nedéléc, H.P. Buchkremer, Properties of bias-assisted sputtered gadolinia-doped ceria interlayers for solid oxide fuel cells, J. Power Sources 195 (2010) 1599–1604, https://doi.org/10.1016/j.jpowsour.2009.09.050.
[31] S.B. Adler, Factors governing oxygen reduction in solid oxide fuel cell cathodes, Chem. Rev. 104 (2004) 4791–4844, https://doi.org/10.1021/cr020724o.
[32] H. Wang, K.J. Yakal-Kremski, T. Yeh, G.M. Rupp, A. Limbeck, J. Fleig, S.A. Barnett, Mechanisms of performance degradation of (La,Sr)(Co,Fe)$O_{3-\delta}$ solid oxide fuel cell cathodes, J. Electrochem. Soc. 163 (2016) F581–F585, https://doi.org/10.1149/2.0031607jes.
[33] A.S. Mehranjani, D.J. Cumming, D.C. Sinclair, R.H. Rothman, Low-temperature co-sintering for fabrication of zirconia/ceria bi-layer electrolyte via tape casting using a Fe_2O_3 sintering aid, J. Eur. Ceram. Soc. 37 (2017) 3981–3993, https://doi.org/10.1016/j.jeurceramsoc.2017.05.018.
[34] H.-J. Choi, Y.-H. Na, M. Kwak, T.W. Kim, D.-W. Seo, S.-K. Woo, S.-D. Kim, Development of solid oxide cells by co-sintering of GDC diffusion barriers with LSCF air electrode, Ceram. Int. 43 (2017) 13653–13660, https://doi.org/10.1016/j.ceramint.2017.07.075.
[35] M. Morales, A. Pesce, A. Slodczyk, M. Torrell, P. Piccardo, D. Montinaro, A. Tarancón, A. Morata, Enhanced performance of gadolinia-doped ceria diffusion barrier layers fabricated by pulsed laser deposition for large-area solid oxide fuel cells, ACS Appl. Energy Mater. 1 (2018) 1955–1964, https://doi.org/10.1021/acsaem.8b00039.
[36] M. Machado, F. Baiutti, L. Bernadet, A. Morata, M. Nuñez, J.P. Ouweltjes, F. C. Fonseca, M. Torrell, A. Tarancón, Functional thin films as cathode/electrolyte interlayers: a strategy to enhance the performance and durability of solid oxide fuel cells, J. Mater. Chem. A 10 (2022) 17317–17325, https://doi.org/10.1039/D2TA03641J.
[37] Y.S. Hong, S.H. Kim, W.J. Kim, H.H. Yoon, Fabrication and characterization GDC electrolyte thin films by e-beam technique for IT-SOFC, Curr. Appl. Phys. 11 (2011) S163–S168, https://doi.org/10.1016/j.cap.2011.03.071.
[38] F.C. Fonseca, S. Uhlenbruck, R. Nédélec, D. Sebold, H.P. Buchkremer, Temperature and bias effects on sputtered ceria diffusion barriers for solid oxide fuel cells, J. Electrochem. Soc. 157 (2010) B1515, https://doi.org/10.1149/1.3476296.
[39] T. Nguyen, K. Kobayashi, T. Honda, Y. Iimura, K. Kato, A. Neghisi, K. Nozaki, F. Tappero, K. Sasaki, H. Shirahama, Preparation and evaluation of doped ceria interlayer on supported stabilized zirconia electrolyte SOFCs by wet ceramic processes, Solid State Ion. 174 (2004) 163–174, https://doi.org/10.1016/j.ssi.2004.06.017.